Magnetic correlations in the two-dimensional repulsive Fermi-Hubbard model

Fedor Šimkovic IV,[1] Youjin Deng,[2] N. V. Prokof'ev,[3,4,*] B. V. Svistunov,[3,4] I. S. Tupitsyn,[3,4] and Evgeny Kozik[1]

[1]*Department of Physics, King's College London, Strand, London WC2R 2LS, United Kingdom*
[2]*Hefei National Laboratory for Physical Sciences at Microscale and Department of Modern Physics,*
University of Science and Technology of China, Hefei, Anhui 230026, China
[3]*Department of Physics, University of Massachusetts, Amherst, Massachusetts 01003, USA*
[4]*National Research Center "Kurchatov Institute," 123182 Moscow, Russia*

The repulsive Fermi-Hubbard model on a square lattice has a rich phase diagram near half-filling ($n = 1$): at $n = 1$ the ground state is an antiferromagnetic insulator, at $0.6 < n \lesssim 0.8$ the ground state is a $d_{x^2-y^2}$-wave superfluid (at least for moderately strong interactions, $U \lesssim 4$), and the region $1 - n \ll 1$ is likely subject to phase separation. Much less is known about the nature of strong magnetic fluctuations at finite temperature and how they change with the doping level. Recent experiments on ultracold atoms have now reached this interesting fluctuation regime. In this work we employ the skeleton diagrammatic method to quantify the characteristic temperature scale $T_M(n)$ for the onset of magnetic fluctuations with a large correlation length.

Introduction. The fermionic Hubbard model [1–4], defined by the square lattice Hamiltonian

$$H = -t \sum_{\langle i,j \rangle \sigma} \hat{c}_{i,\sigma}^\dagger \hat{c}_{j,\sigma} + U \sum_i \hat{n}_{i,\uparrow} \hat{n}_{i\downarrow} - \mu \sum_{i,\sigma} \hat{n}_{i,\sigma}, \quad (1)$$

has for years played a crucial role in studies of correlated electrons in solids; it is regarded as one of the "standard models" of condensed matter physics to introduce and discuss Mott insulating phases, antiferromagnetic (AFM) correlations, novel mechanisms of superconducting pairing, non-Fermi-liquid behavior, etc. In Eq. (1) and in what follows, the nearest-neighbor hopping amplitude t is set to be the energy and temperature unit (distances are measured in units of the lattice constant); U is the on-site repulsive coupling constant; μ is the chemical potential; $\hat{c}_{i,\sigma}^\dagger$ and $\hat{c}_{i,\sigma}$ create and annihilate, respectively, a fermion of the spin component $\sigma \in \{\uparrow, \downarrow\}$ at site i; and $\hat{n}_{i,\sigma}$ counts the number of fermions of a particular spin at a given lattice site.

On the one hand, Eq. (1) involves a number of crucial simplifications that make it qualitatively different from real materials, such as high-T_c superconductors. The most important ones include (i) two-dimensional, as opposed to the strongly anisotropic three-dimensional, geometry; (ii) neglect of long-range Coulomb interactions; (iii) suppression of hopping matrix elements beyond the nearest-neighbor ones ($t' = 0$); (iv) single-band approximation; and (v) absence of electron-phonon coupling. Correspondingly, the model (1) cannot feature an ordered AFM phase at finite temperature but is allowed to have a first-order transition between phases with different electron densities, not to mention that $t' = 0$ leads to the Fermi surface nesting and particle-hole symmetry at $n = \langle \hat{n}_{i\uparrow} + \hat{n}_{i\downarrow} \rangle = 1$. As a result, the schematic phase diagram of (1) in the doping-temperature plane shown in Fig. 1 (see discussion below) is distinct from the "canonical" picture of high-T_c-type materials [4]. On the other hand, advances in ultracold-atomic experiments have made it possible to

accurately emulate the model (1) on optical lattices [5–14]. This remarkable progress brings ultracold-atom experiments into the region of the phase diagram (Fig. 1), where they can cooperate with the state-of-the-art numerical methods to reveal the underlying physics. Numerical results can now be directly compared to experiments (and vice versa), which dramatically increases the importance of producing reliable data sets.

Recent years have seen a remarkable progress in unveiling the $T = 0$ phase diagram of (1). Well-understood regions include the limit of vanishing densities $n \to 0$ [15–21] and vanishing interaction strength [22–25]. For densities $n \leqslant 0.7$ and coupling strength $U \leqslant 4$, the ground state is a BCS superfluid (with $d_{x^2-y^2}$-wave symmetry at density $n > 0.6$) [26]. At half-filling $n = 1$, the ground state is an AFM insulator for any U [27–31]. Being a qualitative property, AFM order can only disappear (with doping) by a quantum phase transition. The simplest scenario is the first-order one, implying phase separation (PS). PS into the insulating AFM and a superfluid is a natural—but still not the only possible—way of doping-driven transitioning between the two ordered ground states. The first PS state was proposed to be a mixture of AFM and ferromagnetic orders in the region of small doping, $\delta = 1 - n \ll 1$, and large U [32–34]; this conjecture was later supported numerically for $U > 25$ [35]. The instability of the model towards incommensurate AFM and domain wall formation was also reported in Refs. [36] and [37]. Recently, PS for small values of U was observed in auxiliary-field quantum Monte Carlo [38,39] and variational [40] studies.

Much less is known conclusively about the finite-temperature behavior. Given that the correlation length ξ for AFM correlations at $n = 1$ diverges exponentially rapidly when $T \to 0$, there exists a relatively high temperature T_M below which magnetic correlations extend over many lattice sites and electronic degrees of freedom are getting locked in collective magnetic modes. The characteristic temperature scale $T_M(n)$ is supposed to decrease with increasing doping level. Since magnetic correlations and fluctuations are considered to be the prime reason for PS and BCS phenomena near half-filling, quantifying their behavior is paramount to
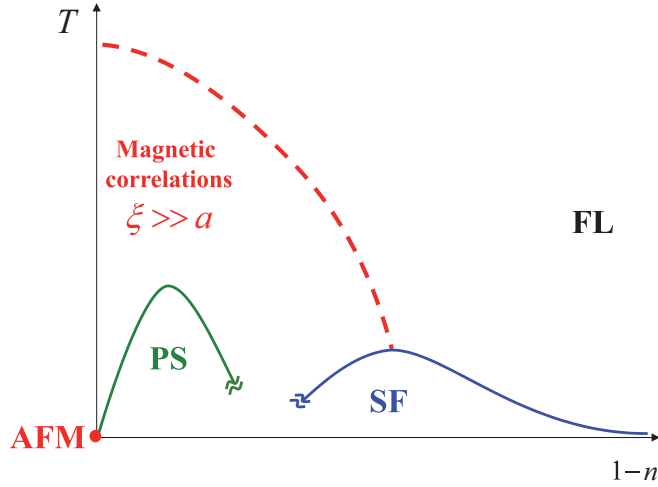
*prokofev@physics.umass.edu

FIG. 1. Schematic phase diagram of the repulsive Fermi-Hubbard model on a square lattice near half-filling, showing the Fermi liquid (FL), superfluid (SF), and putative phase separation (PS) regimes, as well as the antiferromagnetic ground state (AFM) at half-filling. Strong magnetic correlations with large correlation lengths, $\xi \gg a$, are observed below the dashed red line.

understanding the finite-temperature phase diagram of the Fermi-Hubbard model in two dimensions.

In this communication, we employ the skeleton diagrammatic approach to quantify the $T_M(n)$ scale (see Fig. 2) and shed light on the structure of dominant fluctuations. The most recent setups with ultracold ^{6}Li fermions have reached temperatures low enough to directly observe magnetic
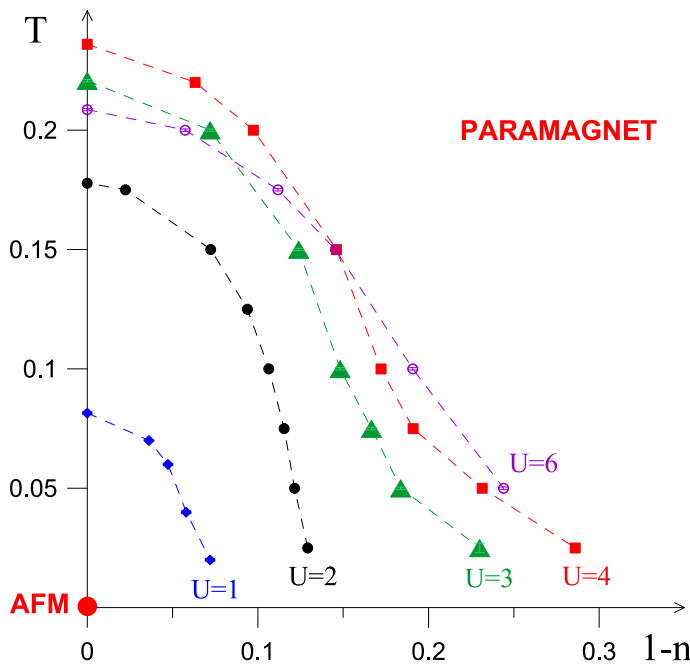

FIG. 2. Onset of strong (incommensurate) magnetic fluctuations as calculated by the lowest-order GGGW method (see text) for values of $1 \leqslant U \leqslant 6$. The region of strong fluctuations increases with U and reaches its maximum at around $U = 4$ at $n = 1$.
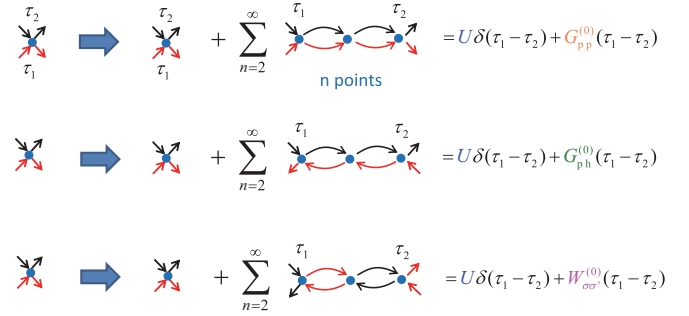

FIG. 3. Simple geometric series that can be constructed by connecting bare interaction vertexes using various pairs of bare single-particle propagators (Green's functions) $G_\sigma^{(0)}$. Red, spin-up propagators; black, spin-down propagators.

correlations in the model (1) [10,12,13], with the lowest temperatures attained on the scale of $T \sim 0.25$ [14].

Method. The imaginary-time spin correlation function $\chi(i,\tau) = \langle S_z(\tau,i)S_z(0,0)\rangle$ and its Fourier transform $\chi(\omega_m,\vec{q})$ at bosonic Matsubara frequencies $\omega_m = 2\pi T m$, where m is an integer, was computed within the skeleton diagrammatic framework based on four fully dressed channels. We start by noting that in any diagram based on bare on-site coupling U every interaction vertex can be "promoted" by adding an infinite sequence based on a particular geometric series (see Fig. 3). This leads to the diagrammatic elements from which an arbitrary Feynman diagram may be constructed by taking any number of diagrammatic elements and connecting their incoming and outgoing ends with propagator lines (see left and right panels in Fig. 4). Note that the particle-particle ladders, $G_{pp}^{(0)}$, particle-hole ladders, $G_{ph}^{(0)}$, and screened interaction, $W_{\sigma\sigma'}^{(0)}$, all have the same structure as the single-particle propagators (Green's functions) $G_\sigma^{(0)}$; i.e., thanks to the local nature of the on-site Hubbard interaction U they depend on only the lattice coordinate and time. In what follows we refer to all G and W functions (bare or fully renormalized) as "lines" and call the U element a "point." The scheme can be abbreviated GGGW, to highlight four renormalization channels.

The necessity of treating the bare interaction point separately originates from precise rules for avoiding double-counting when all diagram lines are assumed to be dressed with the corresponding self-energy insertions. In the skeleton technique, one computes self-energies for all lines in the graph—Σ_σ for G_σ, Σ_{pp} for G_{pp}, Σ_{ph} for G_{ph}, and $\Pi_{\sigma\sigma'}$ for

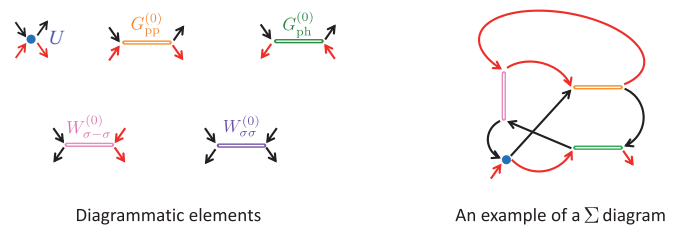Diagrammatic elements   An example of a Σ diagram

FIG. 4. Diagrammatic elements based on ladders and screened interactions (left) and an example of a particular diagram for the single-particle self-energy Σ based on them (right).
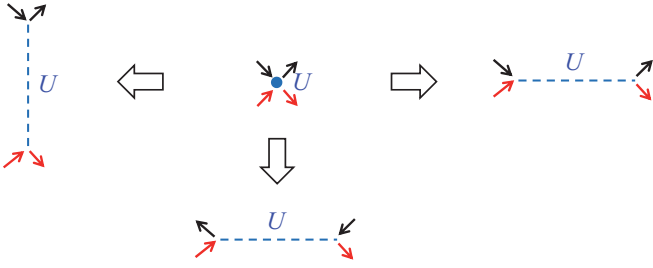
FIG. 5. Three ways of "interpreting" the bare interaction vertex in the context of different channels. In each interpretation the interaction line carries a different momentum.

FIG. 6. First-order skeleton graphs for all self-energies.

$W_{\sigma\sigma'}$—and uses them to "dress"/renormalize the corresponding lines using Dyson equations:

$$G_\sigma = \frac{G_\sigma^{(0)}}{1 - G_\sigma^{(0)}\Sigma_\sigma}, \quad W = \frac{U}{1 - U\Pi} - U, \tag{2}$$

$$G_{pp} = \frac{U}{1 - U\Sigma_{pp}} - U, \quad G_{ph} = \frac{U}{1 - U\Sigma_{ph}} - U. \tag{3}$$

These are simple algebraic relations in the momentum/frequency representation. The spin-spin correlation function is directly related to the polarization Π by

$$\chi(\omega_n,\vec{q}) = \mathrm{Tr}\; S_z \frac{\Pi(\omega_n,\vec{q})}{1 - \Pi(\omega_n,\vec{q})U} S_z, \tag{4}$$

with the trace taken over the spin index.

The self-energy diagrams are computed self-consistently by using the solutions of (2) and (3) for all diagram lines. To avoid double-counting, these diagrams must be from the so-called skeleton set: they remain connected after the cutting of any two lines of the same kind. This is identical to enforcing the rule that no two lines in the free-energy graph have the same momentum; skeleton self-energy diagrams are then obtained by removing one of the lines from the closed free-energy graph. In addition, one has to enforce two rules concerning dots:

(i) No two dots can be connected by two Green's functions.

(ii) Dots cannot be connected to the same end of either G_{pp}, or G_{ph}, or W by two Green's functions in a manner that reproduces their geometrical-series structure.

This is necessary because, by construction, such diagrams are already accounted for in the line definitions when considering their first-order self-energies. By admitting that the bare interaction vertex can be interpreted in three ways (with the corresponding momentum going along the line) as depicted in Fig. 5, we observe that these additional rules are accounted for automatically by the "no two lines carry the same momentum" rule. Finally, there is one exception to the rule: To avoid triple-counting of the same diagram contributing to the lowest-order Σ, one has to perform subtraction of the diagram based on two points (see Fig. 6).

All results in this work are based on the lowest-order diagrams shown in Fig. 6 and the solution of Dyson equations (2) and (3) iteratively. The diagrammatic Monte Carlo scheme for simulating higher-order skeleton graphs (based on standard principles described in previous work [26,41,42], with obvious modifications required to reflect a larger set of diagrammatic elements and self-energies) was only used to establish that the
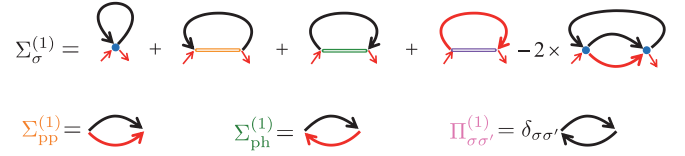
lowest-order scheme was producing accurate thermodynamic results at the level of a few percent. We have also verified this level of accuracy for spin correlations by benchmarking results at $n = 1$ against the sign-free determinant diagrammatic Monte Carlo method [43].

Results. The very notion of T_M as the crossover temperature between the high-temperature regime, with $\xi \leqslant 1$, and the regime of strong magnetic correlations, with $\xi \gg 1$, implies that its definition is not unique. To define the onset of strong magnetic fluctuations we examine the momentum dependence of the static magnetic susceptibility $\chi(0,\vec{q})$ and the development of a narrow peak structure. More precisely, T_M is the highest temperature that results in the peak amplitude's being an order of magnitude larger than the minimum value of χ over the Brillouin zone, $\chi_{\max}/\chi_{\min} = 10$. Our results are summarized in Fig. 2.

As expected, the largest values of T_M (at fixed U) are observed at half-filling, where the crossover temperature can be as high as $T \sim 0.25$ (or about 1000 K in units representative of CuO_2 superconductors with hopping amplitude $t \sim 0.3$ eV [44]). As a function of interaction, T_M goes to 0 at both large and small values of U and, within the considered range of $1 \leqslant U \leqslant 6$, features a smooth maximum around $U \sim 4$. This appears to be the optimal spot for experimental studies of magnetism in (1), where reaching low temperatures remains challenging. The magnetic crossover scale goes to 0 with doping but remains relatively high for intermediate values of U even at doping levels $\delta \in (0.15, 0.25)$. We did not see evidence of PS at T_M, meaning that the PS dome takes place within the magnetic region (see Fig. 1).

The character of spin correlations undergoes a dramatic transformation with doping. A mismatch between the largest momentum transfer at the Fermi surface and the reciprocal lattice vector results in incommensurate spin-wave fluctuations that take the form of AFM domains and *diagonal* domain walls. In Fig. 7, we show a typical example of the emerging structure (for $T = 0.05$, $U = 4$, and $n = 0.8085$). In the left panel, we see that the otherwise dominant peak around the commensurate vector (π,π) is split and features a minimum at (π,π) surrounded by two maxima at the incommensurate vectors. The real-space spin texture behind this split-peak signal is shown in the right panel, with different colors corresponding to the sign of $\chi(0,\vec{r})$. For brevity, we will call it "diagonal stripes." It is plausible that in the putative PS region (see Fig. 1), the AFM order is intermixed with diagonal stripes, and the mechanism for the $d_{x^2-y^2}$-wave pairing is based on coupling to these spin fluctuations.

Conclusions. We have discussed the finite-temperature phase diagram of the repulsive Fermi-Hubbard model on a square lattice and identified the overarching dome defining the onset of strong magnetic correlations that change their
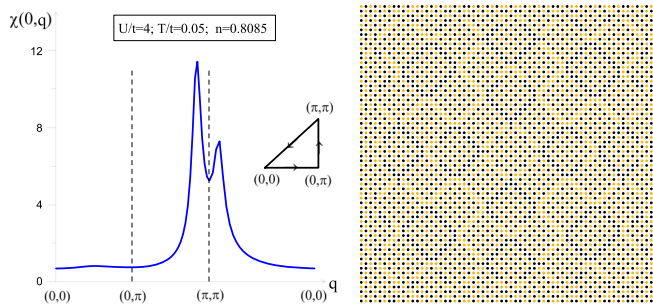
FIG. 7. Left: Static magnetic susceptibility calculated from the lowest-order GGGW diagrams and plotted over the trace $(0,0) \to (\pi,0) \to (\pi,\pi) \to (0,0)$ in the Brillouin zone for $T = 0.05$, $U = 4$, and $n = 0.8085$. Two peaks are observed at the incommensurate vectors (π,Q) and (Q,Q), where Q is some value other than π. Right: The corresponding diagonally striped "carpet" pattern is plotted in real space, with colors reflecting the sign of the average spin correlation. Whether this pattern survives or changes as $T \to 0$ remains an open question.

structure from commensurate antiferromagnetism to incommensurate diagonal stripes as the doping level is increased. Given the relatively high values of T_M that extend well into the doping region, where optimal values for transition temperatures to $d_{x^2-y^2}$ superfluidity are expected to take place, magnetic correlations appear to be the key ingredient behind both the PS and the BCS phenomena near half-filling.

Further development of the diagrammatic Monte Carlo approach is required to obtain controllable results at temperatures below T_M, where convergence of the diagrammatic expansion becomes problematic. A large magnetic correlation length and phase separation are two factors that have to be treated with extreme care by any numerical method based on finite-cluster simulations because they impose restrictions on

the minimal acceptable cluster sizes and call into question the homogeneity of the solution. In particular, superfluid states proposed in [44–46] cannot exist in the parameter space of phase separation. To find high-T_c regions one has to avoid PS near half-filling or modify the model to include nonzero values of the next-nearest-neighbor hopping $t' > 0$ [45].

Ultracold-atom experiments are expected to have a major impact on revealing the finite-temperature phase diagram. Current experiments have already reached temperatures $T \sim T_M$ [14] and are well positioned to explore the structure of strong magnetic correlations. The detection and characterization of the PS state require lower temperature scales, but we do not see any reason for the PS dome to occur at $T \ll T_M$ given that known correlations are becoming saturated below T_M.

Quantifying magnetic correlations is also of significant interest in relation to copper oxides [47], as neutron scattering experiments have revealed the coexistence of commensurate and incommensurate magnetic structures at finite doping. For $La_{2-p}Sr_pCu_4$ an incommensurate state with a magnetic structure wave vector was found at small dopings; for $YBa_2Cu_3O_{6+y}$ a wide doping window exists where commensurate AFM fluctuations are observed at low temperatures [48].

[1] J. Hubbard, in *Proceedings of the Royal Society of London A: Mathematical, Physical and Engineering Sciences* (The Royal Society, London, 1963), Vol. 276, pp. 238–257.

[2] P. W. Anderson, Solid State Phys. **14**, 99 (1963).

[3] P. W. Anderson *et al.*, *The Theory of Superconductivity in the High-Tc Cuprate Superconductors* (Princeton University Press, Princeton, NJ, 1997), Vol. 446.

[4] P. A. Lee, N. Nagaosa, and X.-G. Wen, Rev. Mod. Phys. **78**, 17 (2006).

[5] D. Jaksch, C. Bruder, J. I. Cirac, C. W. Gardiner, and P. Zoller, Phys. Rev. Lett. **81**, 3108 (1998).

[6] M. Lewenstein, A. Sanpera, V. Ahufinger, B. Damski, A. Sen, and U. Sen, Adv. Phys. **56**, 243 (2007).

[7] M. Köhl, H. Moritz, T. Stöferle, K. Günter, and T. Esslinger, Phys. Rev. Lett. **94**, 080403 (2005).

[8] R. Jördens, N. Strohmaier, K. Günter, H. Moritz, and T. Esslinger, Nature **455**, 204 (2008).

[9] U. Schneider, L. Hackermüller, S. Will, T. Best, I. Bloch, T. Costi, R. W. Helmes, D. Rasch, and A. Rosch, Science **322**, 1520 (2008).

[10] R. G. Hulet, P. M. Duarte, R. A. Hart, and T.-L. Yang, *Proceedings of the 22nd International Conference on Laser Spectroscopy (ICOLS2015), Singapore, 28 June 3 July* (2015).

[11] R. A. Hart, P. M. Duarte, T.-L. Yang, X. Liu, T. Paiva, E. Khatami, R. T. Scalettar, N. Trivedi, D. A. Huse, and R. G. Hulet, Nature **519**, 211 (2015).

[12] D. Greif, G. Jotzu, M. Messer, R. Desbuquois, and T. Esslinger, Phys. Rev. Lett. **115**, 260401 (2015).

[13] M. F. Parsons, A. Mazurenko, C. S. Chiu, G. Ji, D. Greif, and M. Greiner, Science **353**, 1253 (2016).

[14] A. Mazurenko, C. S. Chiu, G. Ji, M. F. Parsons, M. Kanász-Nagy, R. Schmidt, F. Grusdt, E. Demler, D. Greif, and M. Greiner, Nature **545**, 462 (2017).

[15] M. Y. Kagan and A. V. Chubukov, JETP Lett. **50**, 517 (1989).

[16] M. A. Baranov and M. Y. Kagan, Z. Phys. B: Condens. Matter **86**, 237 (1992).

[17] A. V. Chubukov and J. P. Lu, Phys. Rev. B **46**, 11163 (1992).

[18] A. V. Chubukov, Phys. Rev. B **48**, 1097 (1993).

[19] D. Zanchi and H. J. Schulz, Phys. Rev. B **54**, 9509 (1996).

[20] C. J. Halboth and W. Metzner, Phys. Rev. Lett. **85**, 5162 (2000).

[21] H. Fukazawa and K. Yamada, J. Phys. Soc. Jpn. **71**, 1541 (2002).

[22] R. Hlubina, Phys. Rev. B **59**, 9600 (1999).

[23] S. Raghu, S. A. Kivelson, and D. J. Scalapino, Phys. Rev. B **81**, 224505 (2010).

[24] A. T. Rømer, A. Kreisel, I. Eremin, M. A. Malakhov, T. A. Maier, P. J. Hirschfeld, and B. M. Andersen, Phys. Rev. B **92**, 104505 (2015).

[25] F. Šimkovic IV, X.-W. Liu, Y. Deng, and E. Kozik, Phys. Rev. B **94**, 085106 (2016).

[26] Y. Deng, E. Kozik, N. V. Prokof'ev, and B. V. Svistunov, Europhys. Lett. **110**, 57001 (2015).

[27] J. E. Hirsch, Phys. Rev. B **31**, 4403 (1985).

[28] J. E. Hirsch and S. Tang, Phys. Rev. Lett. **62**, 591 (1989).

[29] S. R. White, D. J. Scalapino, R. L. Sugar, E. Y. Loh, J. E. Gubernatis, and R. T. Scalettar, Phys. Rev. B **40**, 506 (1989).

[30] N. Furukawa and M. Imada, J. Phys. Soc. Jpn. **61**, 3331 (1992).

[31] C. N. Varney, C.-R. Lee, Z. J. Bai, S. Chiesa, M. Jarrell, and R. T. Scalettar, Phys. Rev. B **80**, 075116 (2009).

[32] D. R. Penn, Phys. Rev. **142**, 350 (1966).

[33] Y. Nagaoka, Phys. Rev. **147**, 392 (1966).

[34] H. Tasaki, Prog. Theor. Phys. **99**, 489 (1998).

[35] R. Zitzler, T. Pruschke, and R. Bulla, Eur. Phys. J. B **27**, 473 (2002).

[36] H. J. Schulz, Phys. Rev. Lett. **64**, 1445 (1990).

[37] H. Q. Lin, Phys. Rev. B **44**, 7151 (1991).

[38] C.-C. Chang and S. Zhang, Phys. Rev. B **78**, 165101 (2008).

[39] S. Sorella, Phys. Rev. B **91**, 241116 (2015).

[40] L. F. Tocchio, F. Becca, and S. Sorella, Phys. Rev. B **94**, 195126 (2016).

[41] K. V. Houcke, E. Kozik, N. Prokof'ev, and B. Svistunov, Phys. Proc. **6**, 95 (2010).

[42] S. A. Kulagin, N. Prokof'ev, O. A. Starykh, B. Svistunov, and C. N. Varney, Phys. Rev. B **87**, 024407 (2013).

[43] E. Burovski, N. Prokof'ev, B. Svistunov, and M. Troyer, Phys. Rev. Lett. **96**, 160402 (2006).

[44] E. Gull, O. Parcollet, and A. J. Millis, Phys. Rev. Lett. **110**, 216405 (2013).

[45] X. Chen, J. P. F. LeBlanc, and E. Gull, Phys. Rev. Lett. **115**, 116402 (2015).

[46] B.-X. Zheng and G. K.-L. Chan, Phys. Rev. B **93**, 035126 (2016).

[47] M. A. Kastner, R. J. Birgeneau, G. Shirane, and Y. Endoh, Rev. Mod. Phys. **70**, 897 (1998).

[48] M. Matsuda, M. Fujita, K. Yamada, R. J. Birgeneau, Y. Endoh, and G. Shirane, Phys. Rev. B **65**, 134515 (2002).